Dongze Wu
Di Li ✉
Xingfeng Liu
Yukuan Li
Yiqun Wang
Shaoxun Liu

https://doi.org/10.21278/TOF.484063324
ISSN 1333-1124
eISSN 1849-1391

TEMPERATURE DEPENDENCE OF MESO CONSTITUTIVE PARAMETERS FOR ADVANCED HIGH-STRENGTH STEEL

Summary

Temperature significantly influences the fracture toughness of dual-phase steel, with internal void damage closely linked to sheet metal fracture. Microstructural damage models are vital for studying material failure, and precise calibration of their parameters is crucial for numerical analysis reliability. This paper focuses on accurately calibrating these parameters using a combination of experimental and numerical simulations based on the Hill'48-Gurson-Tvergaard-Needleman (GTN) model. Employing a central composite experimental design, response surface methodology, and genetic algorithms, the study determines relevant damage parameters for dual-phase steel at different temperatures. The research carefully analyses the evolution patterns of damage parameters concerning sheet metal and corresponding temperatures. The study contributes to understanding damage parameter evolution patterns, offering a predictive method for dual-phase steel sheet damage parameters across varying temperature conditions.

Key words: *advanced high-strength steel; meso-damage model; response surface methodology; temperature dependence*

1. Introduction

Advanced high-strength dual-phase steel (DP) is a pivotal lightweight material widely used in the construction of automotive body structural components. During the warm tensile deformation process of dual-phase steel sheets, the mechanical properties of the material exhibit noticeable dependence on temperature. Merely examining the warm forming process of dual-phase steel from a macroscopic phenomenological perspective has inherent limitations. The damage and fracture occurring during the deformation process are, in reality, highly sensitive to considerations of the physical background of damage and the reflection of microstructural changes within the material. Meso-damage theories, employing averaging methods, establish a connection between the micro-damage processes of the material and the macroscopic fracture processes. This contributes to a more profound understanding of the assessment of material failure processes and their intrinsic physical nature.

Gurson [1] first established the porous damage plasticity potential model, but the author did not consider the influence of factors such as pore nucleation, the interaction between pores, and pore coalescence on the mechanical properties of materials. Building upon the Gurson model, Tvergaard and Needleman [2] improved the Gurson model by introducing pore volume interaction parameters and pore volume fractions, a modification referred to as the GTN model. Abbasi [3] used the GTN model to predict the formability limit of Interstitial-Free steel through finite element simulation. Applying the response surface method of central composite design, the results indicated that the response surface method could be employed to determine the damage parameters in the GTN model. Ying [4], within the temperature range of 600-800 °C, analysed the rheological behaviour of Boron steel 22MnB5 through a series of thermal tensile tests. Based on the response surface method and genetic algorithm, a calibration process for damage parameters was presented. Han [5] employed the Swift flow stress model to formulate the regression equation correlating stress-strain and damage parameters. Through the application of orthogonal tests, Han identified the optimal damage parameters. The findings suggest that parameter 'a' initially experiences an ascent followed by a descent with rising temperatures, while parameter 'b' exhibits a consistent upward trend in relation to temperature increments. The full name of the BP neural network is the Back Propagation neural network, and its core is the BP algorithm, which stands for the error back propagation algorithm [6]. Zhou [7] utilised the GTN microscopic damage model to establish a temperature-dependent damage model for 5A06 aluminium alloy plates subjected to a temperature of 250 °C and a strain rate of 0.01 s-1. Employing a BP neural network, a comprehensive model linking damage parameters to the fracture point was constructed. Through the application of a genetic algorithm, the optimal set of damage parameters was determined. The simulation results were found to be consistent with the experimental results. Henseler [8] determined the nucleation, coarsening, and growth rate mechanisms of voids in AZ31 magnesium within the temperature range of room temperature to 350 °C. In-situ tensile tests were conducted with three different sample types under scanning electron microscopy. Through a comparison analysis of the measured local strains and determined local void volume fractions, material parameters based on the GTN model were experimentally determined. Ding et al. [9], using finite element inverse analysis, scanning electron microscopy, and orthogonal experimental methods, calibrated the GTN damage model parameters f_0, f_c, f_n, and f_f. The validated GTN damage model parameters effectively predicted the fracture failure of 6061 alloy during the tensile process. TINET et al. [10] conducted a high-temperature tensile experiment to analyse the damage evolution mechanism of AISI303 stainless steel, confirming the physical significance of the critical pore volume fraction and failure pore volume fraction in the GTN model. The critical pore volume fraction is influenced by the deformation temperature, stress triaxiality, external load, and rolling angle. Li et al. [11] compared and evaluated the uniaxial tensile test results of AA5182-O aluminium alloy sheets at different strain rates. Through the response surface method, they calibrated the GTN model parameters and studied the impact of the damage parameters on the true stress-strain curve and pore volume evolution. Samir et al. [12] determined damage parameters through tensile test experiments and numerical simulations, optimising the parameters of the GTN model using the response surface method (RSM). The optimised parameters were applied to the numerical analysis of the single point incremental forming process to predict failure, revealing good agreement between the experimental and numerical results. Chen [13], using deep drawing of square box specimens as an example, employed the orthogonal experimental design method to analyse the influence of GTN model damage parameters on the thickness reduction rate and damage degree of aluminium alloy sheets after deep drawing. It was found that the average equivalent plastic strain during pore nucleation had the most significant impact on the results after deep drawing. In summary, the GTN meso-damage model can accurately describe the ductile failure process of tough metallic materials caused by the nucleation, growth, and coalescence of microvoids. Additionally, it can consider the effects of different strengthening criteria and material anisotropy on performance.

Due to the numerous parameters of the GTN model, the tedious determination and validation methods, the complex mathematical derivations, and susceptibility to temperature, the application of the GTN model in engineering practice is directly restricted. [14] Temperature is a primary factor influencing the toughness fracture of dual-phase steel, and the evolution of internal void damage is closely related to sheet metal fracture. Therefore, delving deeper into the study of fracture behaviour at different temperatures requires taking void damage as a starting point. This paper introduces a method for calibrating GTN model parameters by incorporating the Hill'48 yield criterion, fitting the relationship curve between the damage parameters and the temperature. It establishes a predictive method for dual-phase steel sheet damage parameters at different temperatures, analysing the impact of damage parameters on the tensile mechanical properties of the material.

2. The Hill'48-GTN meso-damage model

The GTN damage model is a commonly used constitutive model in material microstructural analysis. To better capture the anisotropic characteristics of the mechanical properties of dual-phase steel sheets, the Hill'48 yield criterion is introduced into the model to enhance the accuracy of numerical simulations for sheet metal failure.

The yield function of the GTN damage model is expressed as Equation (1):

$$\Phi = \left(\frac{\sigma_{eq}}{\sigma_m}\right)^2 + 2q_1 f^* \cosh\left(\frac{3q_2\sigma_h}{2\sigma_m}\right) - \left[1 + q_3 f^{*2}\right] = 0 \tag{1}$$

where σ_{eq} is the Mises equivalent stress, σ_h is the hydrostatic stress, and σ_m is the equivalent stress of the material; q_1, q_2, q_3 are the three interaction parameters of the hole. When q_1=q_2=q_3=1, the GTN damage model degenerates into the Gurson damage model.

f* is the hole volume fraction function as in Equations (2), (3):

$$f^* = \begin{cases} f & f \le f_c \\ f_c + \pi\left(f - f_c\right) & f > f_c \end{cases} \tag{2}$$

$$\pi = \frac{f_u^* - f_c}{f_f - f_c} \tag{3}$$

where f_c is the critical pore volume fraction when the pores start to polymerise, f_f is the pore volume fraction when the material fails, Π is the pore growth acceleration factor, and f_u^* is the value of f* when the stress is 0 in the yield equation. When f*=0, it represents no defects inside the material, and the initial state is f*=f.

For metallic materials containing defects like voids, it is acknowledged that the plastic flow of the material is influenced by the equivalent plastic strain of the matrix and the volume fraction of the voids. To establish a more cohesive link between the micro and macroscopic aspects, the principle of equivalent plastic work is applied, resulting in the expression for the obtained equivalent plastic strain as Equation (4):

$$d\bar{\varepsilon}_p^m = \frac{\sigma : d\varepsilon^p}{\left(1-f\right)\sigma_m} \tag{4}$$

where ε^p is the plastic strain tensor.

To enhance the representation of the mechanical properties of duplex steel sheets featuring diverse anisotropies, the Hill'48 yield criterion is incorporated into the model to refine the accuracy of numerical simulations for sheet failure, as expressed in Equation (5) [15]:

$$F\left(\sigma_{22}-\sigma_{33}\right)^2+G\left(\sigma_{33}-\sigma_{11}\right)^2+H\left(\sigma_{33}-\sigma_{11}\right)^2+2L\sigma_{23}^2+2M\sigma_{31}^2+2L\sigma_{12}^2=\bar{\sigma}^2 \tag{5}$$

where L, M, G, H, N, F denote the anisotropy parameter of the Hill '48 criterion; σ_{11}, σ_{22}, σ_{33} are the hydrostatic normal stress; σ_{23}, σ_{31}, σ_{12} are the deviatoric shearing stress; and $\bar{\sigma}$ represents the equivalent stress. The experimental derivation of L, M, and N is often challenging. Therefore, for practical convenience, L=M=N is usually assumed.

If the Hill'48 yield function is incorporated into the flow law as a plastic potential function, the connection between the plastic strain increment S_{ij} and the stress bias in the case of material adhering to Hill'48 anisotropic yielding can be derived, as show in Equations (6) and (7):

$$\mathrm{d}\varepsilon_{ij}^{\mathrm{p}}=\mathrm{d}\lambda\frac{\partial f}{\partial\sigma_{ij}}=\mathrm{d}\lambda\frac{3}{2}\frac{S_{ij}}{\bar{\sigma}} \tag{6}$$

$$S_{ij}=\frac{1}{F+G+H}\begin{cases}H\left(\sigma_{11}-\sigma_{22}\right)+G\left(\sigma_{11}-\sigma_{33}\right)\\F\left(\sigma_{22}-\sigma_{33}\right)+H\left(\sigma_{11}-\sigma_{22}\right)\\-F\left(\sigma_{22}-\sigma_{33}\right)+G\left(\sigma_{33}-\sigma_{11}\right)\\N\tau_{12}\\M\tau_{31}\\L\tau_{23}\end{cases} \tag{7}$$

In the equations, $\mathrm{d}\varepsilon_{ij}^{p}$ represents the plastic strain increment, $\mathrm{d}\lambda$ is a non-negative proportional coefficient reflecting the relationship between the two, f is the plastic potential function, and S_{ij} represents the plastic strain increment.

3. Experiments

3.1 Test specimen

Systematic temperature tensile tests were conducted on DP590, DP780, DP980, and DP1180 duplex steel sheets using the WDW-20D universal testing machine. The maximum test force of the tensile testing machine is 20 kN. The tensile testing machine is shown in Fig. 1. The sheets, each possessing a consistent thickness of 1 mm, were provided by the company, and their detailed composition is outlined in Table 1. Table 2 offers a comprehensive presentation of the anisotropy parameters associated with these sheet materials, contributing valuable insights into their mechanical behaviour under varying temperature conditions.

Table 1 Composition and mass fraction of sheet metal /%

Steel	C%	Si%	Mn%	P%	S%	Al%
DP590	0.08	0.46	1.75	0.014	0.004	0.032
DP780	0.1	0.16	2.02	0.008	0.003	0.039
DP980	0.179	1.714	2.25	0.01	0	0.029
DP1180	0.118	0.23	2.48	0.008	0.001	0.031

The design of the specimen dimensions was conducted in accordance with the Chinese national standard [16] to better match the grips of the tensile testing machine and enhance the precision of the experiment. Four protrusions were designed on the specimen for easier

clamping based on the actual experimental conditions. The four types of plate material samples were obtained through laser cutting, and their dimensions are as shown in Fig. 2.

Table 2 Sheet anisotropy parameters

Steel	*F*	*G*	*H*	*L*	*M*	*N*
DP590	0.84	1.023	0.98	2.768	2.768	2.768
DP780	0.56	0.56	0.44	1.5	1.5	1.5
DP980	0.4907	0.573	0.427	1.38	1.38	1.38
DP1180	0.46	0.55	0.45	1.46	1.46	1.46

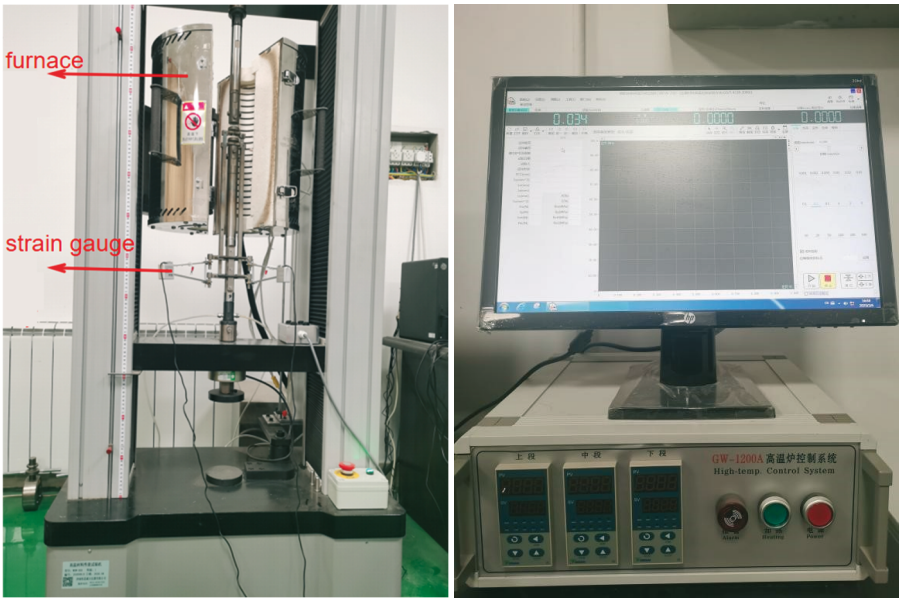

Fig. 1 Tensile test machine

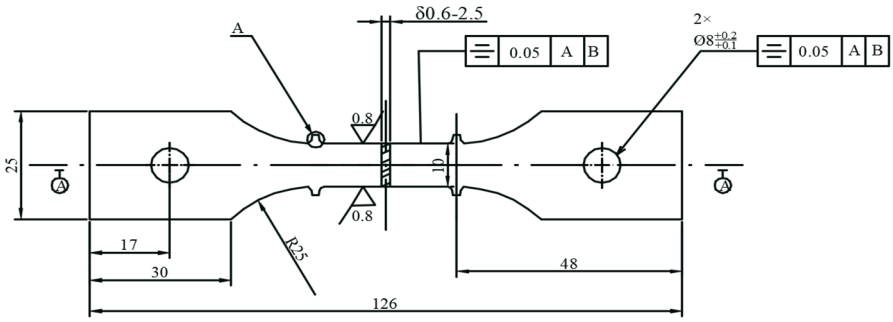

Fig. 2 Dimensions of the uniaxial tensile specimen

3.2 Experimental results

The tensile tests were conducted at temperatures of 200°C, 300°C, 400°C, 500°C, and 600°C, with a tensile rate of 0.1 mm/s. The test procedure was executed until the specimen fractured. The resulting engineering stress-strain curves were then converted to true stress-strain curves, as depicted in Fig. 3.

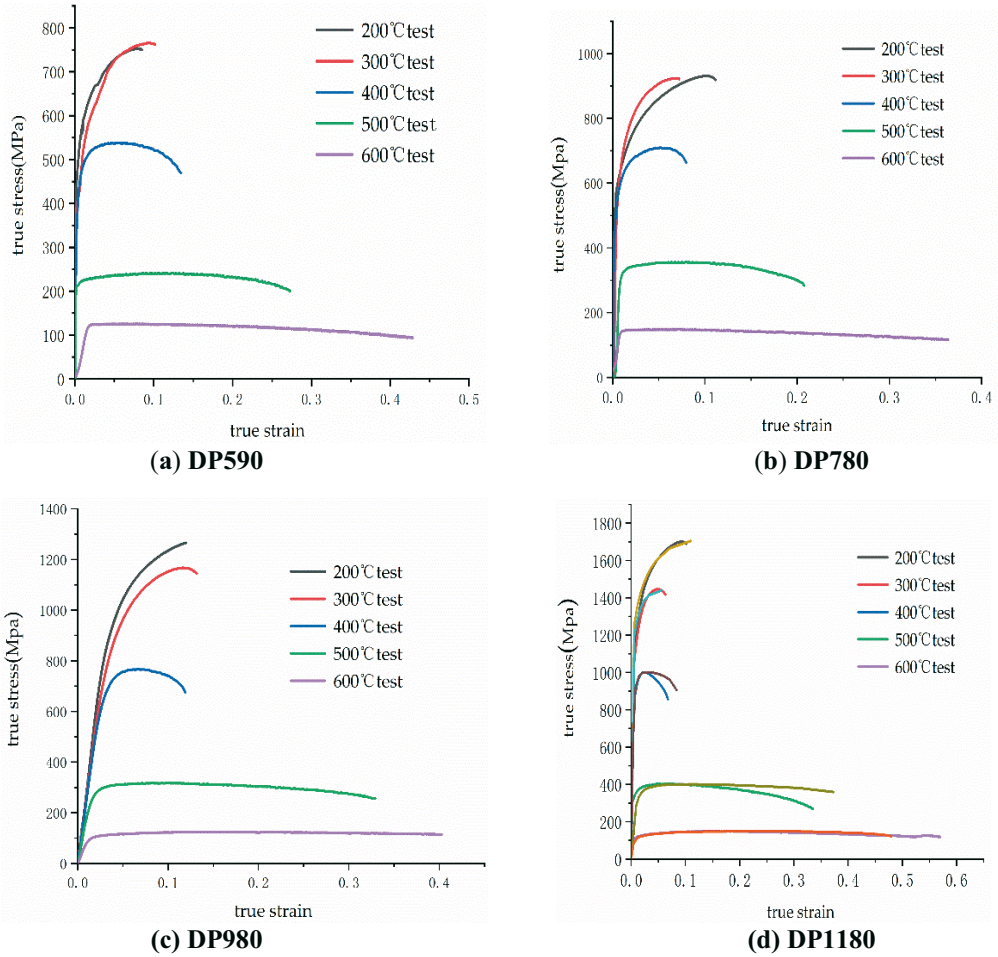

Fig. 3 True stress-strain curve of dual-phase steel

3.3 Identification of Swift model hardening parameters

To ascertain the mechanical and hardening properties of the four sheet materials at varying temperatures, the widely recognised Swift model was employed to describe the mechanical characteristics of the sheets [17]. The model's expression is presented in Equation (8):

$$\sigma=K(\varepsilon_0+\bar{\varepsilon}_p)^n \tag{8}$$

where K represents the hardening coefficient, ε_0 is the pre-strain, n is the hardening index and $\bar{\varepsilon}_p$ is the plastic strain.

The real stress-strain curve is chosen from the initiation of the plastic region to the tensile strength, and the plastic curve is fitted using the least-squares method to determine the values of K and n. The initial trends in the performance parameters for duplex steel plate material are established: the hardening coefficient of duplex steel plate material rises with the strength of the plate material and declines with the increasing temperature, indicating a notable softening effect with rising temperatures. Simultaneously, the hardening index decreases with the increase in both the strength and temperature of the duplex steel plate material.

4. Calibration of meso-damage parameters in the GTN model

4.1 Yield surface coefficient calibration

After checking the literature, it is evident that the majority of references have established the yield surface coefficients q_1, q_2, q_3 as 1.5, 1, and 2.25, respectively. Therefore, this paper adopts the same numerical values.

4.2 Calibration of the pore nucleation coefficient

According to the research of Liu [18], We [19], Xu [20], and others, the average nucleation strain is determined based on the strain value when strain localisation occurs in tensile specimens at different temperatures. For the room temperature forming of dual-phase steel, the standard deviation of nucleation strain (ε_n) remains set at 0.1. The adopted values determined in this study are shown in Table 3.

Table 3 The value of ε_n of the four sheet materials at different temperatures

Temperature	DP590	DP780	DP980	DP1180
200 ℃	0.26	0.26	0.26	0.26
300 ℃	0.27	0.258	0.255	0.258
400 ℃	0.32	0.318	0.316	0.315
500 ℃	0.333	0.325	0.322	0.318
600 ℃	0.338	0.333	0.326	0.323

4.3 Calibration of pore damage parameters

The pore damage parameters in the GTN model are primarily denoted as f_0, f_c, f_n, and f_f, corresponding to the initial pore parameter, critical pore volume fraction, the nucleating particle pore volume fraction, and the failed pore volume fraction. In this paper, we employ finite element analysis to inversely determine the pore damage parameters. The specific process is as follows.

(1) Finite element simulation model

A finite element simulation model is established based on the actual dimensions of the specimen. A refined mesh is employed for the gauge section, with a mesh size of 0.5 mm, while the remaining portions have a mesh size of 2 mm. The element type used is C3D8R. The material properties are determined based on the relevant damage parameters, and the loading and boundary conditions are defined.

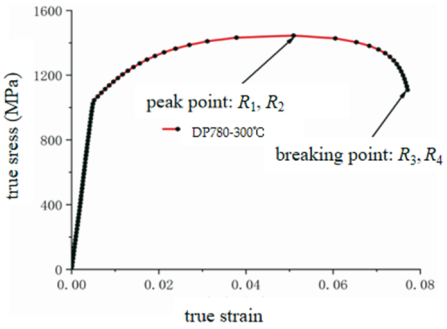

Fig. 4 Critical position of the damage point

(2) Central composite experimental design

The peak and fracture points on the tensile curve, as depicted in Fig. 4, are considered crucial locations for damage investigation [21]. If the data points obtained through numerical simulation align with the peak and fracture points on the experimental curve, a simulation curve that closely matches the experimental curve can be achieved.

Based on the previous literature review and finite element simulation, taking the calibration of damage parameters under 400 ℃ for DP590 dual-phase steel as an example, the coefficient levels of the damage parameters obtained from the central composite experimental design are presented in Table 4.

Table 4 Injury parameter coefficient level

Damage parameter	Low level	High level	Mean value
f_0	0.004	0.008	0.006
f_c	0.01	0.036	0.024
f_n	0.012	0.03	0.024
f_f	0.078	0.12	0.1

Sequentially simulating the levels of the above factors, the corresponding strain at the peak point (R_1), stress at the peak point (R_2), strain at the fracture point (R_3), and stress at the fracture point (R_4) were obtained. The obtained response values are presented in Table 5.

Table 5 Simulation results of the central composite experiment design

	Experimental factors				Response value			
Test number	f_0	f_c	f_n	f_f	R_1	R_2	R_3	R_4
1	0.008	0.01	0.03	0.07	0.0137736	530.187	0.151236	523.561
2	0.008	0.01	0.012	0.12	0.16138	532.745	0.243302	504.56
3	0.004	0.028	0.03	0.12	0.166478	540.409	0.325321	510.752
4	0.004	0.028	0.03	0.07	0.166478	540.409	0.249236	532.763
5	0.004	0.028	0.012	0.12	0.16671	540.915	0.385083	500.7
6	0.006	0.019	0.021	0.095	0.164199	536.079	0.242894	526.549
7	0.006	0.019	0.021	0.095	0.164199	536.079	0.242894	526.549
8	0.006	0.019	0.021	0.145	0.164199	536.079	0.312808	501.598
9	0.008	0.01	0.03	0.12	0.138357	528.187	0.150263	524.782
10	0.006	0.019	0.003	0.095	0.165118	537.365	0.373271	519.705
11	0.008	0.028	0.012	0.07	0.160978	532.706	0.237119	522.327
12	0.01	0.019	0.021	0.095	0.0177223	508.353	0.208841	501.481
13	0.006	0.001	0.021	0.095	0.03206	538.635	0.134534	478.65
14	0.004	0.01	0.012	0.07	0.16671	540.915	0.248931	533.146
15	0.008	0.01	0.03	0.07	0.0137736	530.187	0.151236	523.561
16	0.008	0.01	0.012	0.12	0.16138	532.745	0.243302	504.56
17	0.004	0.028	0.03	0.12	0.166478	540.409	0.325321	510.752
18	0.004	0.028	0.03	0.07	0.166478	540.409	0.2492361	532.763
19	0.004	0.028	0.012	0.12	0.16671	540.915	0.385083	500.7
20	0.006	0.019	0.021	0.095	0.164199	536.079	0.242894	526.549
21	0.006	0.019	0.021	0.095	0.164199	536.079	0.242894	526.549
22	0.006	0.019	0.021	0.145	0.164199	536.079	0.312808	501.598
23	0.008	0.01	0.03	0.12	0.138357	528.187	0.150263	524.782
24	0.006	0.019	0.003	0.095	0.165118	537.365	0.373271	519.705
25	0.008	0.028	0.012	0.07	0.160978	532.706	0.237119	522.327
26	0.01	0.019	0.021	0.095	0.0177223	508.353	0.208841	501.481
27	0.006	0.001	0.021	0.095	0.03206	538.635	0.134534	478.65
28	0.004	0.01	0.012	0.07	0.16671	540.915	0.248931	533.146

(3) Establishing response surface models

To more accurately determine the damage parameters at different temperatures, a second-order polynomial model is selected for regression analysis between the damage parameters and the chosen response values [22]. The general form of the selected model is typically Equation (9):

$$Y = a_0 + \sum_{i=1}^{4} a_i X_i + \sum_{i=1}^{4} a_{ii} X_i^{\ 2} + \sum_{i=1}^{3} \sum_{j=i+1}^{4} a_{ij} X_i X_j \tag{9}$$

where Y represents the response value, a_0, a_i, a_j, a_{jj}, a_{ii} represent the intercept and coefficients for different order terms, and X_iX_j represents the damage parameters.

Through regression analysis, for example for the response value R_1, the P-values for f_c and f_n are both < 0.1. Following the method, significant damage values are selected, thus constructing appropriate second-order polynomial regression equations for different response values. After analysis, the regression equations established for DP590 dual-phase steel at 400 °C are as follows (Equations 10-13):

$$\begin{aligned} R_1 = {} & 0.2001 + 0.0014 f_0 + 0.1009 f_c - 0.0537 f_n + 0.0025 f_f - 0.0829 f_0 f_c + 0.035 f_0 f_n \\ & + 0.0274 f_0 f_f + 0.0513 f_c f_n + 0.0497 f_n f_f - 0.0468 f_0^{\ 2} - 0.0434 f_n^{\ 2} \end{aligned} \tag{10}$$

$$\begin{aligned} R_2 = {} & 536.49 - 7.59 f_0 - 1.12 f_c - 1.64 f_n - 0.7125 f_f - 3.11 f_0 f_c - 1.57 f_0 f_n - 0.5327 f_0 f_f \\ & + 0.9713 f_c f_f - 3.94 f_0^{\ 2} \end{aligned} \tag{11}$$

$$\begin{aligned} R_3 = {} & 0.2685 - 0.017 f_0 + 0.0824 f_c - 0.0377 f_n + 0.0192 f_f - 0.0215 f_0 f_c + 0.036 f_0 f_n \\ & - 0.0136 f_0 f_f + 0.0589 f_c f_n \end{aligned} \tag{12}$$

$$\begin{aligned} R_4 = {} & 543.1 + 21.69 f_0 + 40.91 f_c + 11.24 f_n - 9.54 f_f - 20.35 f_0 f_c + 31.4 f_0 f_n + 5.29 f_0 f_f \\ & + 35.91 f_c f_n + 12.06 f_n f_f - 16.77 f_0^{\ 2} - 5.65 f_n^{\ 2} \end{aligned} \tag{13}$$

Through an analysis of variance, as indicated in Table 6, it can be observed that the regression model exhibits good fitness.

Table 6 Regression equation R^2 analysis results

	R_1	R_2	R_3
Model P-value	<0.0001	<0.0001	<0.0001
Model R^2	96.79%	96.36%	96.39%
Model signal-to-noise ratio	19.4	26.75	27.67
CV value	9.87%	0.38%	6.88%

(4) Genetic algorithm solving parameters

Using MATLAB software and the GATBX toolbox, with the corresponding regression equation as the fitness function, the quality of individuals in the population is evaluated through the fitness function, and genetic algorithms are employed to solve the damage parameters. The final determined damage parameters for four types of plates at different temperatures are shown in Tables 7-10.

Table 7 DP590 sheet void damage parameters

DP590	f_0	f_c	f_n	f_f
200℃	0.007	0.01	0.08	0.03
300℃	0.0075	0.009	0.078	0.032
400℃	0.0063	0.02	0.1	0.028
500℃	0.0017	0.034	0.11	0.023
600℃	0.00152	0.046	0.12	0.011

Table 8 DP780 sheet void damage parameters

DP780	f_0	f_c	f_n	f_f
200℃	0.007	0.013	0.08	0.036
300℃	0.0075	0.0118	0.073	0.034
400℃	0.0063	0.0195	0.1	0.025
500℃	0.00187	0.028	0.113	0.021
600℃	0.00153	0.039	0.125	0.0118

Table 9 DP980 sheet void damage parameters

DP980	f_0	f_c	f_n	f_f
200℃	0.007	0.011	0.076	0.032
300℃	0.0075	0.0108	0.0792	0.033
400℃	0.0063	0.0198	0.106	0.027
500℃	0.00227	0.0312	0.109	0.0226
600℃	0.007	0.011	0.076	0.032

Table 10 DP1180 sheet void damage parameters

DP980	f_0	f_c	f_n	f_f
200℃	0.007	0.0145	0.08	0.0285
300℃	0.0075	0.0123	0.071	0.036
400℃	0.0062	0.018	0.12	0.0247
500℃	0.00267	0.027	0.135	0.02
600℃	0.0011	0.038	0.137	0.0188

5. Prediction and verification of pore damage parameters

The distribution of hole damage parameters for duplex steel at various temperatures is illustrated in Fig. 5. Initially, the hole damage parameters for the four types of sheet materials exhibit minimal sensitivity to temperature. However, the critical hole volume fraction and the failure hole volume fraction both display an increasing and then a decreasing trend with temperature, reaching an inflection point at approximately 300 ℃. Simultaneously, the formable nucleation volume fraction demonstrates an increasing and then decreasing pattern with the rising temperature, also reaching an inflection point at about 300 ℃. It can be inferred that a higher critical pore volume fraction contributes to delaying hole polymerization, a greater volume fraction of failure holes delays the initiation of sheet rupture, and enhances material plasticity and elongation after fracture. The increase in the nucleation volume fraction accelerates damage evolution, leading to earlier material failure. By considering the tensile curves of the four types of duplex steel and test results, it is observed that duplex steel plates exhibit a blue brittle phenomenon in the temperature range of 300 ℃-400 ℃, accompanied by poor elongation and plasticity performance. Subsequently, as the

temperature increases, all four types of plate materials show a significant improvement in elongation and plasticity. Therefore, it is evident that the evolution of pore damage parameters and the variation in plate plasticity for the four types of duplex steel at different temperatures follow a similar pattern.

On comparing the stress-strain curves at various temperatures for the four types of sheet materials, it is evident that the maximum error value among the stress-strain curves for these materials is 5.8%. Consequently, the calibrated damage parameters can be deemed accurate. To enhance the determination of the hole-related damage parameters at different temperatures and to streamline the calibration process, relationship curves between the damage parameters and temperature are fitted.

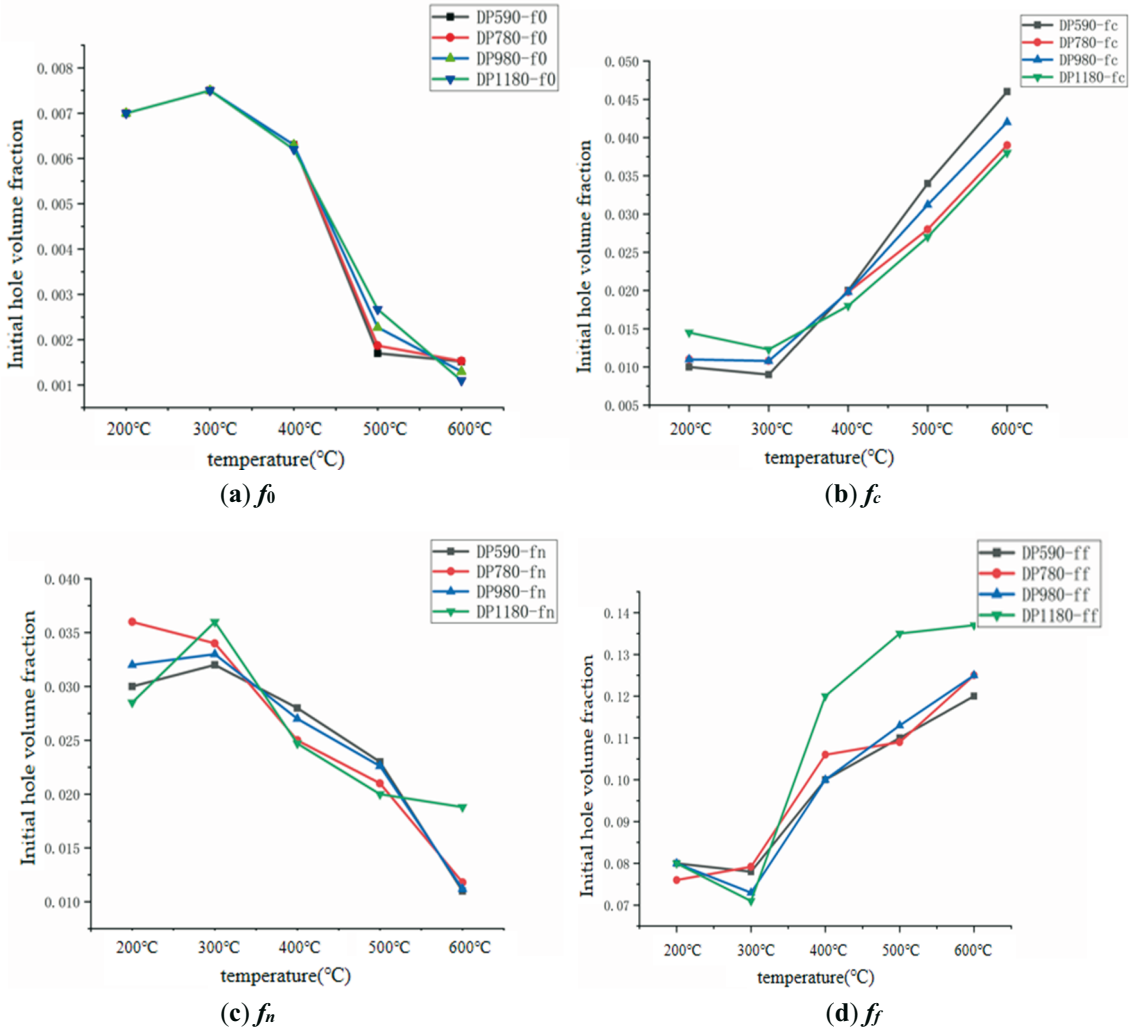

(a) f_0 (b) f_c

(c) f_n (d) f_f

Fig. 5 Change pattern of void damage parameters

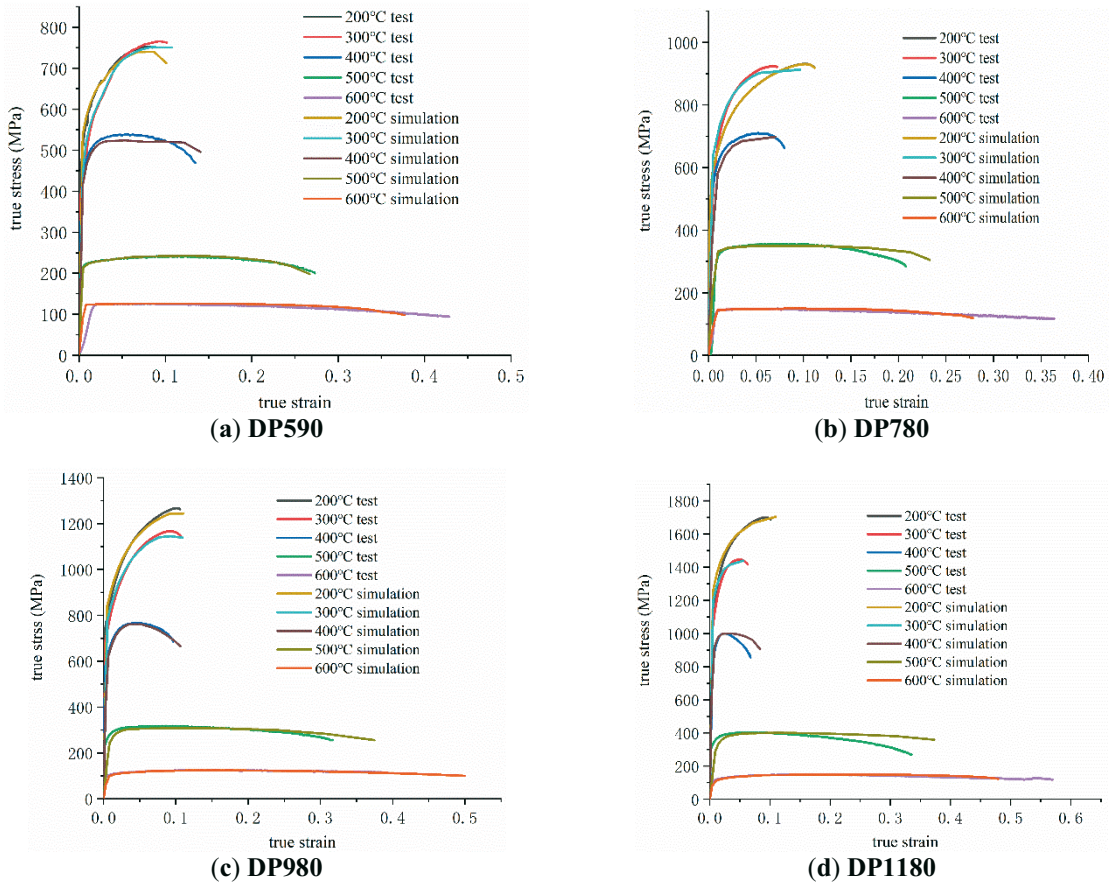

Fig. 6 Simulation comparison of real stress-strain curve test of dual-phase steel

Initial void volume fraction f_0:

$$f_0 = 0.00606 + 1.45e^{-5} \times T - 3.89e^{-8} \times T^2 \tag{14}$$

Critical pore volume fraction f_c:

$$f_c = 0.01889 - 7.73e^{-5} \times T + 1.93e^{-7} \times T^2 \tag{15}$$

Nucleating particle pore volume fraction f_n:

$$f_n = 0.02206 + 8.01e^{-5} \times T - 1.62e^{-7} \times T^2 \tag{16}$$

Failed pore volume fraction f_f:

$$f_f = 0.2 - 0.00121 \times T + 3.56e^{-6} \times T^2 - 2.93e^{-9} \times T^3 \tag{17}$$

Fig. 7 illustrates the simulation results for DP590 at a temperature of 500 °C. Initially, the damage values are low during the stretching process, and the evolution is relatively gradual. As stretching continues, the increase in the overall pore volume fraction accelerates upon reaching the nucleation volume fraction. Subsequently, upon reaching the critical volume fraction, the damage further accelerates. The growth rate of the pore nucleation volume fraction increases with the equivalent plastic strain. Ultimately, the volume fraction of pores in complete failure is 0.108, aligning with the evolution pattern predicted by the GTN model. Fig. 8 presents a simulation comparison of the stress-strain test for DP780 at a temperature of 550 °C. In conclusion, it can be affirmed that the prediction of fine-scale damage parameters for dual-phase steel is accurate.

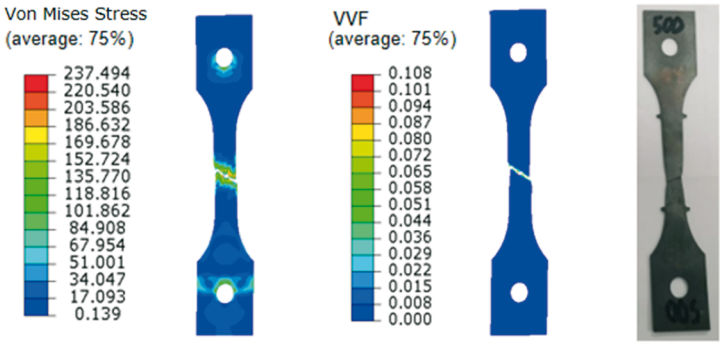

Fig. 7 DP590 500 °C simulation results

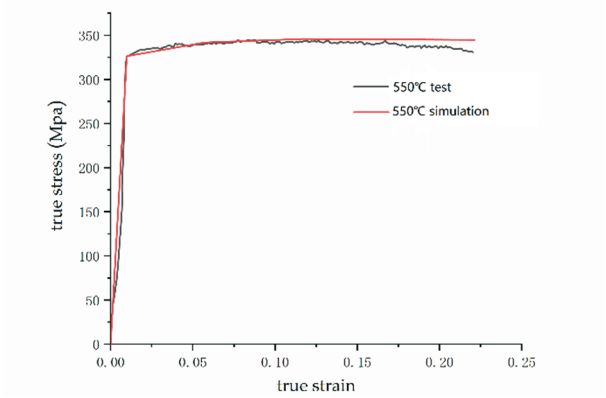

Fig. 8 DP780 550 °C stress-strain curve test simulation comparison

To delve into the specific evolution of hole damage, Fig. 9 presents the hole damage distribution of DP590 duplex steel under 400 °C. In Stage 1, with minimal displacement, the hole damage values across the specimen are uniformly distributed and small. Progressing to Stage 2, as the displacement increases, the damage value at the centre of the specimen surpasses that at the two sides, signifying that plastic deformation predominantly occurs in the middle of the specimen. Advancing to Stage 3, when the displacement approaches tensile rupture, the damage becomes concentrated in the centre of the specimen. Upon reaching the fraction of failure holes, the simulation, utilising the unit elimination method, indicates the occurrence of fracture at this point.

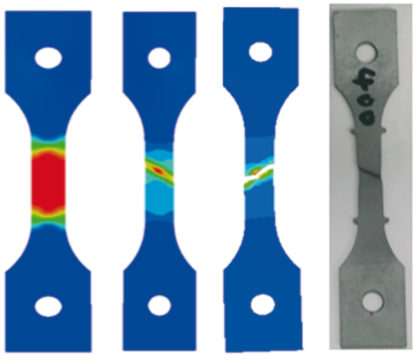

Fig. 9 The hole damage distribution of DP590 400 °C. (a) First stage, (b) Second stage, (c) Third stage, (d) Specimen

Fig. 10 illustrates the trend in hole volume fraction variation with equivalent plastic strain in the central unit of the specimen extracted at different temperatures. Observing the evolution of hole damage, it becomes evident that sheets with higher yield strength experience earlier

damage evolution. Additionally, a higher temperature and superior sheet grades, characterised by better elongation, contribute to delayed hole damage evolution. Regarding the impact of temperature on the evolution of damage, it is notable that elevated temperatures significantly enhance plate plasticity, resulting in a slower occurrence of hole damage.

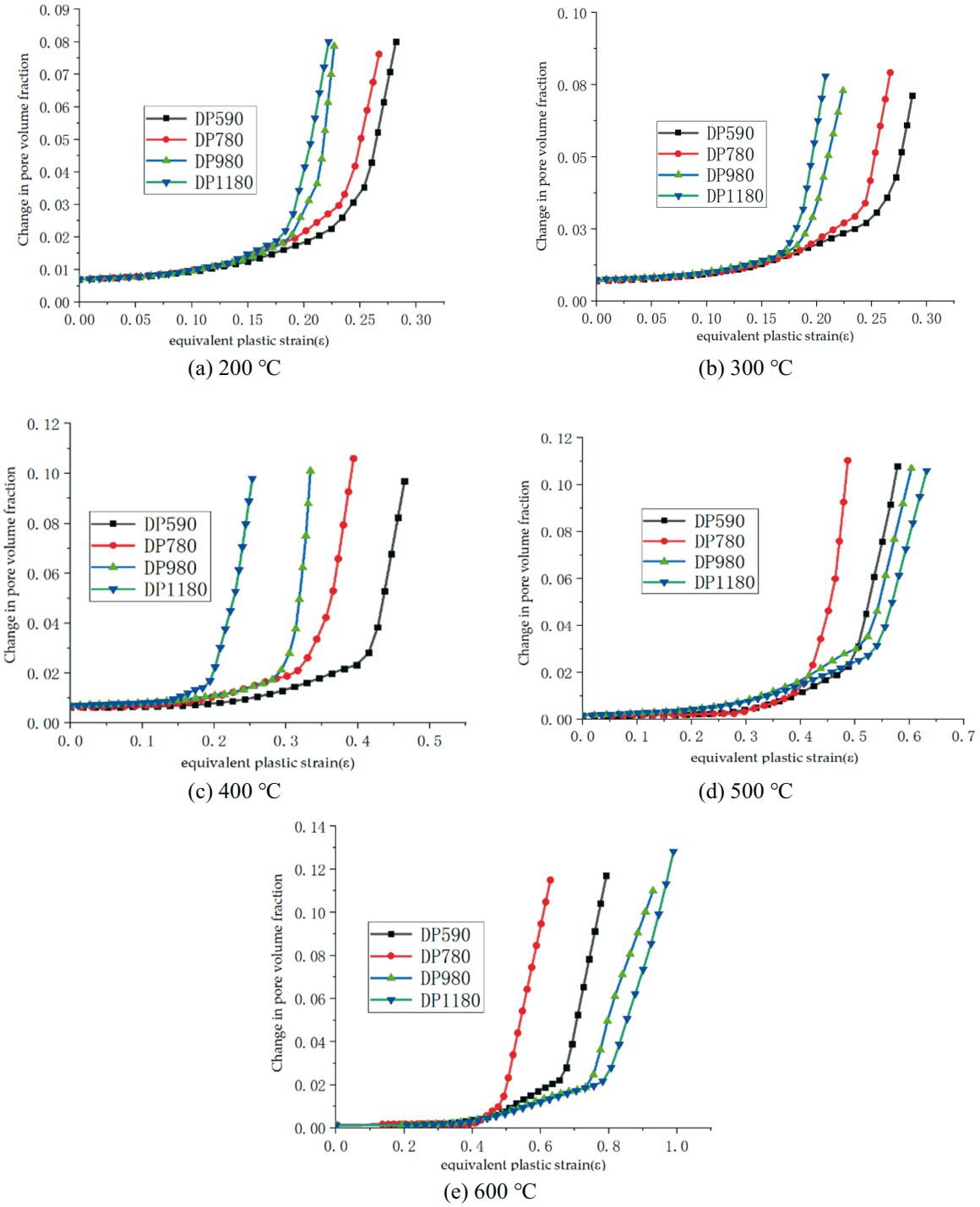

(a) 200 °C (b) 300 °C

(c) 400 °C (d) 500 °C

(e) 600 °C

Fig. 10 Plots of the void volume fraction change at different temperatures

6. Conclusions

In this study, our focus is on four types of duplex steel sheet materials. Given the complexity of the GTN model and the need for calibration based on experimental data, multiple damage parameters, possibly in combination, must be accurately determined. To achieve

precise calibration, we employ a test-centred composite design-response surface method-genetic algorithm-numerical simulation approach to calibrate the damage parameters of the four plate materials at various temperatures. We establish a prediction method for damage parameters in duplex steel plate materials under different temperature conditions.

By comparing stress-strain curves obtained from both tests and simulations, we validate that the damage parameters derived from the GTN model provide a more accurate simulation of the temperature-dependent tensile behaviour of duplex steel. Notably, the impact of temperature on the initial pore damage parameters of the four types of plates is minimal. The critical pore volume fraction and failure pore volume fraction for these plates exhibit a tendency to increase and then decrease with temperature, while the volume fraction of formable nuclei shows a corresponding trend of increase and decrease with temperature.

Acknowledgements

Thanks to RONGCHENG COMPAKS NEW ENERGY AUTOMOBILE CO., LTD, for supporting the joint development project.

REFERENCES

[1] Gurson, A. L. (1977). Continuum theory of ductile rupture by void nucleation and growth: Part I—Yield criteria and flow rules for porous ductile media. https://doi.org/10.1115/1.3443401

[2] Needleman, A., & Tvergaard, V. (1991). An analysis of dynamic, ductile crack growth in a double edge cracked specimen. International Journal of Fracture, 49, 41-67. https://doi.org/10.1007/BF00013502

[3] Abbasi, M., Shafaat, M. A., Ketabchi, M., Haghshenas, D. F., & Abbasi, M. (2012). Application of the GTN model to predict the forming limit diagram of IF-Steel. *Journal of Mechanical science and Technology*, *26*, 345-352. https://doi.org/10.1007/s12206-011-1038-z

[4] Ying, L., Liu, W., Wang, D., & Hu, P. (2017). Parameter calibration of GTN damage model and formability analysis of 22MnB5 in hot forming process. Journal of Materials Engineering and Performance, 26, 5155-5165. https://doi.org/10.1007/s11665-017-2962-6

[5] M. Han, D. Li, K. D. Wang, J. C. Xu, & N. Jiang. (2022). Determination of microscopic damage parameters and temperature dependence of high-strength duplex steel DP780. Journal of Applied Mechanics, 38(5), 2064-2068. https://doi.org/10.11776/cjam.38.05.B013 (In Chinese)

[6] Bakirtzis A G, Petridis V, Kiartzis S J, et al. A neural network short term load forecasting model for the Greek power system. IEEE Transactions on power systems, 1996, 11(2): 858-863. https://doi.org/10.1109/ 59.496166

[7] P. Zhou, R. Y. Zhu, C. Shi, L. Deng, X. Y. Wang, & G.F. Chen (2021). Warm-forming damage modeling of 5A06 aluminum alloy based on GTN model. Journal of Plasticity Engineering, 27(12), 164-169. https://doi.org/10.3969/j.issn.1007-2012.2020.12.023 (In Chinese)

[8] Henseler, T., Osovski, S., Ullmann, M., Kawalla, R., & Prahl, U. (2020). GTN model-based material parameters of AZ31 magnesium sheet at various temperatures by means of SEM in-situ testing. *Crystals*, *10*(10), 856. https://doi.org/10.3390/cryst10100856

[9] Ding, F., Hong, T., Xu, Y., & Jia, X. (2022). Prediction of fracture behavior of 6061 aluminum alloy based on GTN model. *Materials*, *15*(9), 3212. https://doi.org/10.3390/ma15093212

[10] Tinet, H., Klöcker, H., & Le Coze, J. (2004). Damage analysis during hot deformation of a resulfurised stainless steel. *Acta materialia*, *52*(13), 3825-3842. https://doi.org/10.1016/j.actamat.2004.04.032

[11] Li, G., & Cui, S. (2020). Meso-mechanics and damage evolution of AA5182-O aluminum alloy sheet Based on the GTN model. *Engineering Fracture Mechanics*, *235*, 107162. https://doi.org/10.1016/j.engfracmech.2020.107162

[12] More, S., Kumar, A., & Narasimhan, K. (2022). Parameter identification of GTN damage model using response surface methodology for single point incremental sheet forming of IF steel. Advances in Materials and Processing Technologies, 8(2), 1753-1768. https://doi.org/10.1080/2374068X.2021.1874770

[13] Z. Y. Chen, & X. H. Dong, (2012). Influence of GTN meso-damage model parameters on the damage behavior of plate materials. Forging Technology, 37(3), 23-27. https://doi.org/10.3969/j.issn.1000-3940.2012.03.006 (In Chinese)

[14] C. F. Sun, D. Li, L. X. Zhao, &, J. C. Xu (2015). Determination of damage parameters for advanced high-strength duplex steel. Agricultural Equipment and Vehicle Engineering, 53(12), 10-13. https://doi.org/10.3969/j.issn.1673-3142.2015.12.003 (In Chinese)

[15] Ludwik, P. (1909). Elemente der technologischen Mechanik. Springer. https://doi.org/10.1007/978-3-662-40293-1

[16] GB/T 4338-2006, Method for High-Temperature Tensile Testing of Metal Materials[S]. China: General Administration of Quality Supervision, Inspection and Quarantine of the People's Republic of China, Standardization Administration of China, 2006.

[17] Swift H W. Plastic instability under plane stress. *Journal of the Mechanics and Physics of Solids*, 1952,1(1): 1-18. https://doi.org/10.1016/0022-5096(52)90002-1

[18] W. Q. Liu. (2018). “Research on Mechanical Behavior and Formability Prediction of Hot Stamping Damage Evolution”, Ph.D. dissertation, Dalian University of Technology, China, Dalian. (In Chinese)

[19] Y. Wen. (2020). “Study of metal plastic forming and its numerical simulation based on ductile damage mechanics”, Ph.D. dissertation, University of Science and Technology, China, Beijing. https://doi.org/10.26945/d.cnki.gbjku.2020.000157 (In Chinese)

[20] M. Xu. (2022). “Research on high temperature damage evolution of 7075 aluminum alloy based on GTN model”, Master's thesis, Jilin University, China, Jilin. https://doi.org/10.27162/d.cnki.gjlin.2022.006805 (In Chinese)

[21] J. K. Huang. (2009). “Fine-scale damage modeling and ductile fracture criterion for metal forming processes”, Ph.D. dissertation, Shanghai Jiao Tong University, China, Shanghai. (In Chinese)

[22] L. Li, S. Zhang, Q. He, et al. (2015). Application of Response Surface Methodology in Experimental Design and Optimization. Laboratory Research and Exploration, 34(08), 41-45. (In Chinese)

Submitted: 08.01.2024

Accepted: 14.6.2024

Dongze Wu
Di Li*
Xingfeng Liu
Yukuan Li
Yiqun Wang
School of Transportation and Vehicle Engineering, Shandong University of Technology, Zibo, China
Shaoxun Liu
Rongcheng Compaks New Energy Automobile Co., Ltd, Rongcheng, China
*Corresponding author:
hahali@sdut.edu.cn